Cellular and Mitochondrial Dual-Targeted Organic Dots with Aggregation-Induced Emission Characteristics for Image-Guided Photodynamic Therapy

Guangxue Feng, Wei Qin, Qinglian Hu, Ben Zhong Tang, and Bin Liu**

Targeted delivery of drugs toward mitochondria of specific cancer cells dramatically improves therapy efficiencies especially for photodynamic therapy (PDT), as reactive oxygen species (ROS) are short in lifetime and small in radius of action. Different from chemical modification, nanotechnology has been serving as a simple and nonchemical approach to deliver drugs to cells of interest or specific organelles, such as mitochondria, but there have been limited examples of dual-targeted delivery for both cells and mitochondria. Here, cellular and mitochondrial dual-targeted organic dots for image-guided PDT are reported based on a fluorogen with aggregation-induced emission (AIEgen) characteristics. The AIEgen possesses enhanced red fluorescence and efficient ROS production in aggregated states. The AIE dot surfaces are functionalized with folate and triphenylphosphine, which can selectively internalize into folate-receptor (FR) positive cancer cells, and subsequently accumulate at mitochondria. The direct ROS generation at mitochondria sites is found to depolarize mitochondrial membrane, affect cell migration, and lead to cell apoptosis and death with enhanced PDT effects as compared to ROS generated randomly in cytoplasm. This report demonstrates a simple and general nanocarrier approach for cellular and mitochondrial dual-targeted PDT, which opens new opportunities for dual-targeted delivery and therapy.

1. Introduction

Mitochondria are the vital subcellular organelles to eukaryotic cells and powerhouse of cell activity.[1,2] Mitochondrial medicine has emerged as a new field of biomedical and pharmacological research.[3] To achieve the mitochondrial targeting with enhanced therapeutic effects, the therapeutic reagents need to be internalized into targeted cells and accumulate at mitochondrial sites.[4–6] Direct modification of drugs or active molecules with mitochondria-targeting ligands has been prevalent in last decades to direct drug cargoes to mitochondria.[7–13] However, these approaches required tedious synthetic processes with the limitation that the postmodified drugs or molecules may not be able to maintain their therapeutic effects.[14] Recently, nanotechnology or nanocarrier systems have been considered as a simple and nonchemical approach to deliver drug molecules to specific targeted cells or subcellular organelles of interest with enhanced stability and pharmacokinetics.[14–19] Up to now, various nanocarriers including liposome micelles or solid nanoparticles (NPs) have been reported to be able to deliver the loaded drugs to mitochondria.[20–27] Several efforts have also been applied to enhance cellular or tumor uptake of the mitochondria-targeted nanocarriers by introducing octaarginine or pH-responsive liposomes at surface,[28–31] but none of them possesses the selectivity toward different cell lines. Recently, Wu et al. reported a strategy to encapsulate porphyrin derivatives by micelles with cellular targeting ability to deliver the load to specific-cell mitochondria.[32] However, it requires the modification of the load (e.g., porphyrin with triphenylphosphnium) to gain the mitochondria-targeting ability. As a consequence, a more general strategy to develop NP systems, which simultaneously possess

G. Feng, Dr. Q. Hu, Prof. B. Liu
Department of Chemical and Biomolecular Engineering
National University of Singapore
Singapore 117585, Singapore
E-mail: cheliub@nus.edu.sg
G. Feng
Environmental Research Institute
National University of Singapore
Singapore 117411, Singapore
W. Qin, Prof. B. Z. Tang
Department of Chemistry and Division of Biomedical Engineering
Hong Kong University of Science and Technology
Clear Water Bay, Kowloon, Hong Kong
E-mail: tangbenz@ust.hk
Prof. B. Z. Tang
SCUT-HKUST Joint Research Laboratory
Guangdong Innovative Research Team
State Key Laboratory of Luminescent
Materials and Devices
South China University of Technology
Guangzhou 510640, China
Prof. B. Liu
Institute of Materials Research and Engineering
Agency for Science
Technology and Research (A*STAR)
Singapore 117602, Singapore

DOI: 10.1002/adhm.201500431

the cellular and mitochondrial dual-targeting capabilities, is highly desirable for existing therapeutic reagents without any chemical modification.

Photodynamic therapy (PDT) utilizing photosensitizers (PSs), light, and oxygen to kill cancer cells has served as a safe and invasive treatment for cancers.[33–38] PSs are able to absorb light energy and generate reactive oxygen species (ROS) that are toxic to tumor.[39–42] As the therapeutic effect only occurs at sites with the presence of both PSs and light irradiation, the side effects toward surrounding health tissues are minimized. However, due to the short lifetime (<0.04 μs) and limited radius of action (<0.02 μm) of singlet oxygen,[12,43–45] the therapeutic effect of PDT is largely affected by the localization of PSs inside cells. Selective targeting toward the most critical subcellular organelles is therefore highly desirable to achieve high anticancer response.[39,46–49] As mitochondria are reported to be the main target of ROS and their damage occurs at the early stage of PDT-induced apoptosis,[50–52] direct targeting PSs to cancer-cell mitochondria largely enhanced anticancer PDT activities.[51–54] For example, porphyrin derivatives have been widely reported in mitochondria-targeted PDT.[12,52,55,56] However, due to the large hydrophobicity of most PSs, they naturally aggregate in aqueous media or when they are accumulated in mitochondria with limited spaces. The aggregation-caused quenching (ACQ) effect of traditional PSs often leads to quenched fluorescence as well as reduced ROS generation,[57–59] which largely compromised the efficiencies of PDT. Moreover, the existence of ACQ effect also makes it difficult to develop NPs with bright fluorescence and efficient ROS production for image-guided PDT based on traditional PSs. Since aggregation is an inevitable process for hydrophobic PSs in biological systems, a new class of PSs with enhanced phototoxicity as well as brighter fluorescence in aggregated state is highly desirable.

Recently, a novel fluorescent probe system based on fluorogens with aggregation-induced emission (AIEgens) characteristics has been developed by us and others.[60–66] It has attracted great research interests in biological and biomedical applications. These AIEgens such as tetraphenylethene (TPE) are propeller shaped, which emit almost no fluorescence when molecularly dissolved but could be induced to become highly emissive in aggregate state due to the prohibition of energy dissipation and restriction of intramolecular rotation (RIR).[62,67–70] The unique feature of AIEgens has made them valuable in the development of lightup probes,[13,71–73] and ultrabright organic dots[74–79] for sensing and imaging applications. Very recently, we and others also found that several AIEgens show efficient ROS production in aggregate state.[72,80–82] These unique properties are ideal for mitochondria-targeted PDT as the accumulation of AIEgens in mitochondria or encapsulation of AIEgens by mitochondria-targeted nanocarriers will not compromise their fluorescence and ROS generation.

In this contribution, we synthesized a new AIEgen and fabricated organic dots with bright red fluorescence and high ROS generation for cellular and mitochondrial dual-targeted PDT. The new AIEgen, DPBA–TPE, shows characteristic AIE features. Under light illumination, the molecules emit strong red fluorescence and could efficiently generate ROS in aggregates. The corresponding AIE dots were then fabricated by a modified nanoprecipitation method using lipid-PEG as encapsulation matrix. Bearing folic acid and triphenylphosphine (TPP) targeting ligands at the surface, the yielded FA–AIE–TPP dots are able to selectively internalize into folate-receptor (FR) positive cancer cells over other cells and subsequently accumulate in mitochondria. The dual-targeted FA–AIE–TPP dots showed enhanced PDT effects as compared to sole cellular targeted or mitochondria-targeted AIE dots. Our NP formulation thus represents a simple and general strategy for cellular and subcellular dual-targeted delivery.

2. Results and Discussion

To demonstrate the potential of AIE dots for cellular and mitochondrial dual-targeted image-guided PDT, we synthesized a new AIEgen, DPBA–TPE (**Scheme 1**). 3,3′-(2,5-Dimethoxy-1,4-phenylene)bis(2-(4-bromophenyl)acrylonitrile) (**5**) was prepared by Knoevenagel reaction from 2,5-dimethoxybenzene-1,4-dicarboxaldehyde (**3**) and bromophenylacetonitrile (**4**) under basic conditions. The final product was obtained with satisfactory yields by the reaction between intermediate (**5**) and aryl amine (**10**) under basic conditions. The purified products were characterized by ^{1}H NMR spectrum (Figure S1, Supporting Information) and mass spectrum (Figure S2, Supporting Information), respectively, which indicate the correct chemical structure and high purity of the obtained DPBA–TPE. In addition, DPBA–TPE possesses good solubility in organic solvents, including tetrahydrofuran (THF), chloroform, dichloromethane (DCM), and toluene, but is insoluble in water.

The structure of DPBA–TPE (Scheme 1) is comprised of the dimethoxybenzene and arylamines as the electron donor (D), cyano groups as the acceptor (A), as well as TPE groups as the iconic AIE unit. The introduction of D–A system to TPE groups is expected to generate a new AIEgen with increased electronic conjugation, and hence longer absorption and emission wavelengths. DPBA–TPE in THF showed an absorption spectrum peaked at 480 nm. The AIE properties of DPBA–TPE were studied by measuring its photoluminescence (PL) spectrum changes in water/THF mixtures with different water fractions (f_w) (**Figure 1**a). DPBA–TPE in THF shows weak orange–red fluorescence where the emission peaks at 619 nm. With the increase of f_w (≤40%), the emission of DPBA–TPE is decreased and bathochromically shifted to 624 nm, due to solvent polarity increase and the transformation to the twisted intramolecular charge transfer (TICT) state. Upon further increasing f_w, the emission of DPBA–TPE is invigorated from f_w of ≈50% and is further intensified. Collectively, these data indicate that DPBA–TPE possesses both AIE and TICT characteristics, while AIE plays a dominant role in determining their optical properties in aggregated states.

To study whether DPBA–TPE is able to generate ROS in aggregated state, dichlorofluorescein (DCFH) was used as the ROS indicator, which initially shows no fluorescence in aqueous solution but emits bright green fluorescence upon reaction with singlet oxygen. As shown in Figure 1b, the mixed aqueous solution of DPBA–TPE (10×10^{-6} M) and DCFH (2×10^{-6} M) showed quickly increased fluorescence centered at 530 nm

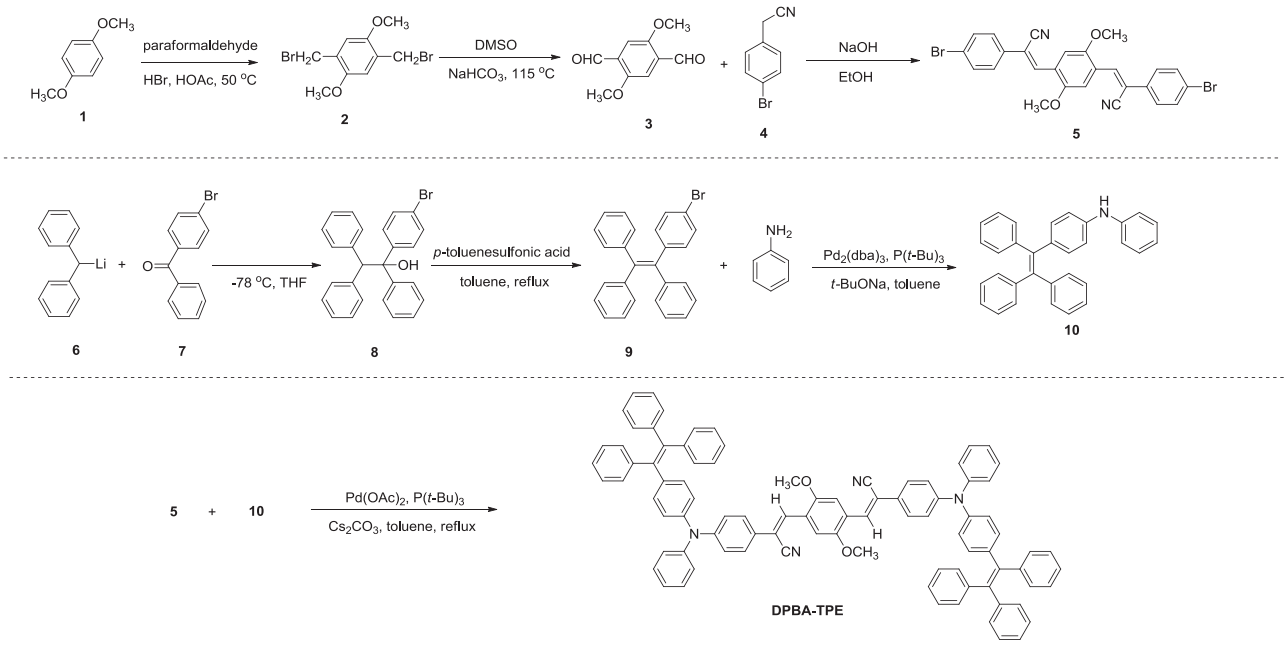

Scheme 1. Synthetic routes to DPBA–TPE.

upon exposure to white light irradiation (250 mW cm^{-2}) within minutes, while DCFH itself under light irradiation remain weakly fluorescent, indicating that the DPBA–TPE aggregates are able to efficiently generate singlet oxygen species. Together with the bright red fluorescence in the aggregated state, it is highly predictable that the encapsulation of DPBA–TPE into organic dots will not compromise its imaging quality and PDT effects.

To fabricate the dual-targeting AIE dots, a modified nanoprecipitation method was used (**Scheme 2**). Biocompatible block copolymers of lipid-PEG with different terminal groups, (1,2-distearoyl-*sn*-glycero-3-phosphoethanolamine-*N*-[amino(polyethylene glycol)-2000]) (DPSE–PEG–NH_2) and (1,2-distearoyl-*sn*-glycero-3-phosphoethanolamine-*N*-[folate(polyethylene glycol)-2000]) (DSPE–PEG–FA) were chosen as the encapsulation matrix due to their high loading efficiency, excellent colloidal stability of the formed dots, as well as the ability to introduce surface functional groups.[83,84] To form the AIE dots, THF solution containing molecularly dissolved DPBA–TPE, DPSE–PEG–NH_2, and DSPE–PEG–FA was diluted into MilliQ water, immediately followed by ultrasound sonication using a microtip sonicator at a power output of 12 W for 120 s. During the mixing and sonication, the hydrophobic DSPE segments will interact and intertwine

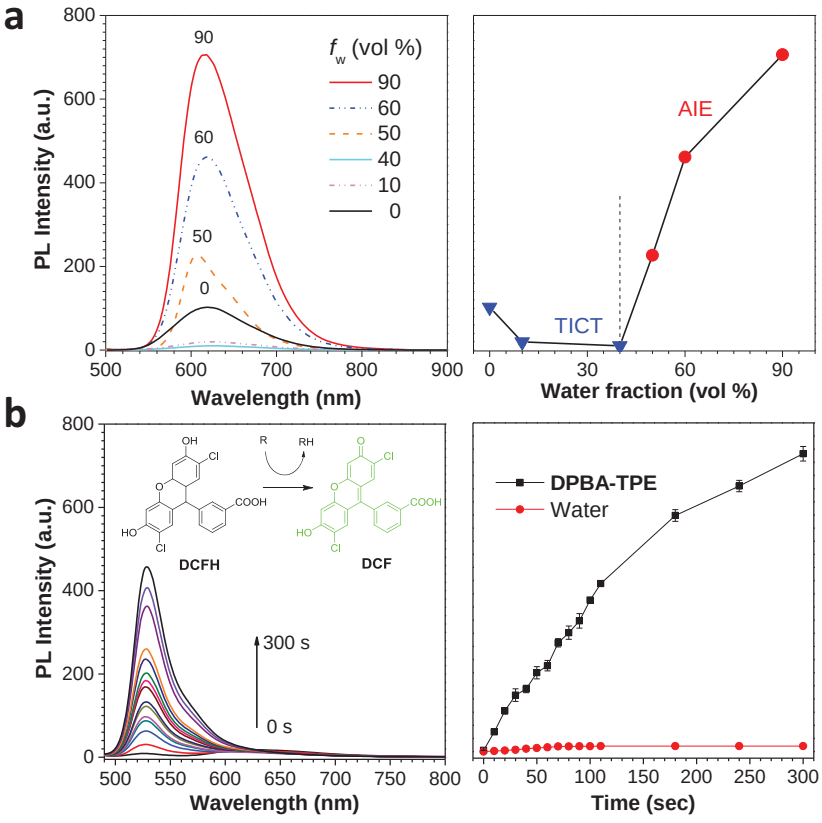

Figure 1. a) PL spectra of DPBA–TPE (10×10^{-6} M) in THF/water mixtures with different water fractions. b) PL spectra of DPBA–TPE (10×10^{-6} M) and DCFH (2×10^{-6} M) mixture in water with different white light irradiation time (250 mW cm^{-2}).

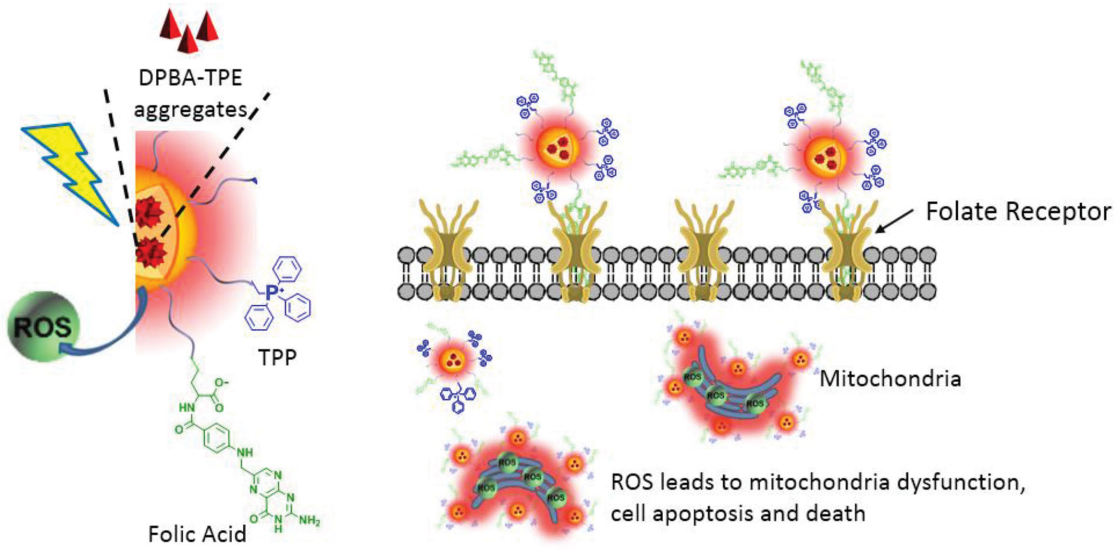

Scheme 2. Schematic illustration of FA–AIE–TPP dots for specific targeting of FR-positive MCF-7 breast cancer-cell mitochondria for image-guided PDT.

with the hydrophobic DPBA–TPE to form the core, while the hydrophilic PEG segments will extend outside toward water phase to form the protective shell. The presence of PEG shells not only stabilizes the AIE dots but also provides the surface amino groups for further conjugation. To bring the AIE dots to mitochondria, cationic TPP, which is able to accumulate in mitochondria in response to high mitochondrial membrane potential (MMP),[85,86] was then reacted with AIE dot suspension to yield FA–AIE–TPP dots. After the reaction, dialysis of the FA–AIE–TPP dots suspension against water using 6 to 8 kDa membrane is applied to remove excess TPP. Similar procedures were applied to fabricate folic acid monofunctionalized AIE dots (AIE–FA) and TPP monofunctionalized AIE dots (AIE–TPP). The formed FA–AIE–TPP dots are expected to specifically internalize into folate receptor (FR) positive cancer cells, and subsequently accumulate in mitochondria for mitochondrial imaging and enhanced PDT effects (Scheme 2).

The absorption and PL spectra of FA–AIE–TPP dots in aqueous suspension are shown in **Figure 2**a. The FA–AIE–TPP dot suspension showed two absorption peaks centered at 305 and 497 nm, respectively. The PL spectrum is centered at 624 nm with a fluorescence quantum yield of 14% using 4-(dicyanomethylene)-2-methyl-6-(p-dimethylaminostyryl)-4H-pyran (DCM) in methanol as reference (43%). It should be noted that surface modification does not affect the optical properties of the AIE dots as both AIE–FA and AIE–TPP dots showed similar absorption and PL spectra (Figure S3, Supporting Information), which should be benefited from the excellent encapsulation ability of lipid-PEG. The hydrodynamic diameters of the three AIE dots were evaluated using dynamic light scattering (DLS). As shown in Figure 2b, AIE–FA, AIE–TPP, and FA–AIE–TPP dots exhibit similar sizes of around ≈30 ± 1.2, ≈35 ± 1.7, and ≈34 ± 1.5 nm with narrow size distribution, respectively (Figure S4, Supporting Information). The surface zeta potentials of the three dots are –9.8, 36.9, 28.9 mV for AIE–FA, AIE–TPP and FA–AIE–TPP dots, respectively. The increase of surface charge of AIE–TPP and FA–AIE–TPP dots should be due to the conjugation of TPP at dots surface, which

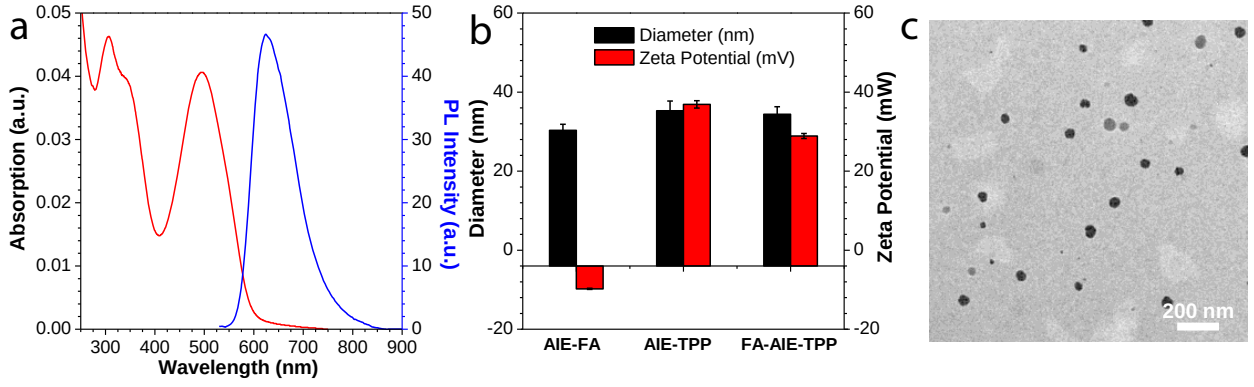

Figure 2. a) Absorption and PL spectra of FA–AIE–TPP dots in water. b) Hydrodynamic diameters and surface zeta potentials of three AIE dots in water. c) TEM image of FA–AIE–TPP dots.

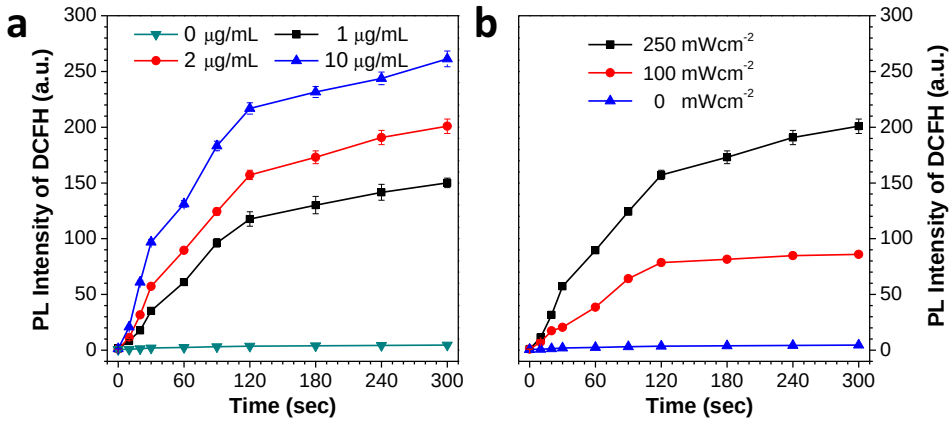

Figure 3. ROS generation of FA–AIE–TPP dots in aqueous solution at a) varied dot concentrations with a fixed light power of 250 mW cm^{-2}, and b) varied light powers with fixed dot concentration of 2 μg mL^{-1} upon irradiation for 300 s, using DCFH (2×10^{-6} M) as ROS indicator.

also slightly increases the AIE dot sizes. High-resolution transmission electron microscope (HR-TEM) was further applied to study the morphology and size distribution of these AIE dots. The FA–AIE–TPP dots are spherical in shape with a mean diameter of 31 nm (Figure 2c), and AIE–FA and AIE–TPP dots exhibit similar spherical shapes (Figure S5, Supporting Information) with sizes around 28 and 32 nm, respectively. In addition, no precipitation was observed after the AIE dots have been stored for several months, indicating the excellent colloidal stability.

The PDT effect of the AIE dots is further studied by measuring the ROS generation efficiency under light irradiation using DCFH as an indicator. As shown in **Figure 3**, the FA–AIE–TPP dot suspension is able to generate ROS very quickly and efficiently under white light irradiation, which is evidenced by the rapid increase of DCFH fluorescence intensity at 530 nm. Moreover, increasing the exposure time, AIE dot concentration, or light power will also increase the ROS generation (Figure 3), indicating that ROS production of AIE dots is time-, concentration-, and power-dependent. Such an efficient ROS generation capability makes the AIE dots a good candidate for image-guided PDT.

The cellular and mitochondrial targeting capabilities of the three AIE dots were investigated by fluorescence imaging. FR-positive MCF-7 breast cancer cells were chosen as the target, with FR-negative NIH-3T3 fibroblast cells as the control. After incubating both cell lines for 4 h with the three AIE dots at 20 μg mL^{-1} based on DPBA–TPE mass concentration, the images were acquired by confocal laser scanning microscope (CLSM). **Figure 4** shows the corresponding fluorescence images of these AIE dots treated either MCF-7 or NIH-3T3 cells. For FA–AIE–TPP or AIE–FA dots incubated cells, much stronger red fluorescence can be observed for MCF-7 cells than NIH-3T3 cells, revealing the targeting capability of folate decorated AIE dots toward FR-positive cells. While, AIE–TPP dots show very weak fluorescence inside both cell lines. Flow cytometry was further applied to

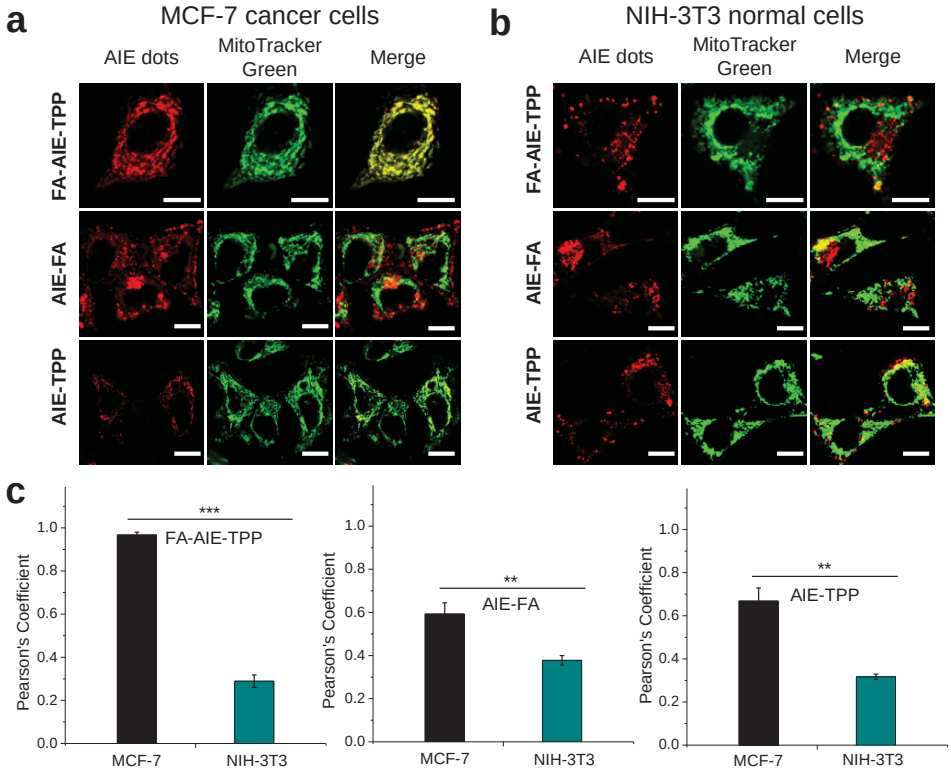

Figure 4. CLSM images of a) MCF-7 cancer cells and b) NIH-3T3 normal cells after incubation with AIE dots (20 μg mL^{-1}) and MitoTracker Green (200×10^{-6} M). AIE dots: E_x: 543 nm, E_m: >650 nm; MitoTracker Green: E_x = 488 nm, E_m = 505–525 nm. c) Pearson's coefficients between AIE dots and MitoTracker Green inside MCF-7 and NIH-3T3 cells. **: $p < 0.001$; ***: $p < 0.0001$. The scale bar size is 10 μm for all images.

the cellular uptake of AIE dots in MCF-7 and NIH-3T3 cells (Figure S6, Supporting Information). All the three AIE dots treated NIH-3T3 cells only show very small increase in average fluorescence intensity, indicating the low cellular uptake of all the AIE dots into NIH-3T3 cells due to lack of cellular-targeting ligands and the suppressed nonspecific internalization by PEG. On the other hand, FA–AIE–TPP and AIE–FA dots treated MCF-7 cells show similar average fluorescence intensities, which are much higher than those of blank or AIE–TPP dots treated MCF-7 cells. The flow cytometry results are consistent with CLSM images, indicating that folic acid decoration promotes the cellular uptake of AIE dots to FR-positive cells. As TPP is able to drive FA–AIE–TPP dots to mitochondria, the similar cellular uptake between AIE–FA dots and FA–AIE–TPP dots should provide insights into the important roles of the PS localization inside cells for different PDT performance.

To test whether these AIE dots are able to accumulate at mitochondrial sites, commercially available mitochondrial tracker MitoTracker Green (Invitrogen) was used as the costain. The red fluorescence from FA–AIE–TPP dots clearly shows a characteristic mitochondrial network inside MCF-7 cells (Figure 4a), which is consistent with green fluorescence emitted from MitoTracker Green. Without TPP decoration, AIE–FA dots are randomly distributed inside MCF-7 cancer cells, indicating that the existence of TPP drives the accumulation of AIE dots to mitochondria. Due to the poor cellular uptake of AIE–TPP dots as previously described, poor visualization of mitochondrial pattern in MCF-7 cells is observed. On the other hand, besides very weak red fluorescence, its poor overlap with the green fluorescence from MitoTracker green is observed for NIH-3T3 cells, indicating the poor cellular uptake and mitochondrial localization of all three AIE dots in FR-negative cells. The Pearson's correlation coefficients are also used to quantify the colocalization between AIE dots and MitoTracker Green (Figure 4c and Figure S7, Supporting Information), which are 0.97, 0.49, and 0.63 for MCF-7 cells, and 0.29, 0.40, and 0.31 for NIH-3T3 cells, for FA–AIE–TPP, AIE–FA, and AIE–TPP dots, respectively. The higher Pearson's coefficient of AIE–TPP dots in MCF-7 than NIH-3T3 cells should be ascribed to the higher mitochondrial membrane potential of cancer cells over normal cells, which promoted mitochondrial accumulation of AIE–TPP dots in MCF-7 cells.[13,89] The highest Pearson's coefficient for FA–AIE–TPP dots toward MCF-7 cell mitochondria clearly demonstrates that modifying the mitochondria-targeted nanocarriers with secondary cellular-targeting ligands is able to enhance their cellular uptake toward targeted cells with subsequent mitochondrial accumulation.

The PDT effects of the three AIE dots on viabilities of NIH-3T3 and MCF-7 cells were then investigated by MTT assays. Upon incubation with the three AIE dots in dark for 24 h, both NIH-3T3 and MCF-7 cells exhibit high cell viabilities of over 90% even at a high DPBA–TPE concentration of 80 μg mL^{-1} (Figure S8, Supporting Information), indicating the low cytotoxicity of AIE dots without light irradiation. In the parallel experiments, incubating both cell lines with AIE dots for 4 h and followed by light irradiation (100 mW cm^{-2}) for 10 min leads to large differences in cell viabilities (**Figure 5**a–c). All three AIE dots exhibit very low phototoxicity toward NIH-3T3 cells, which

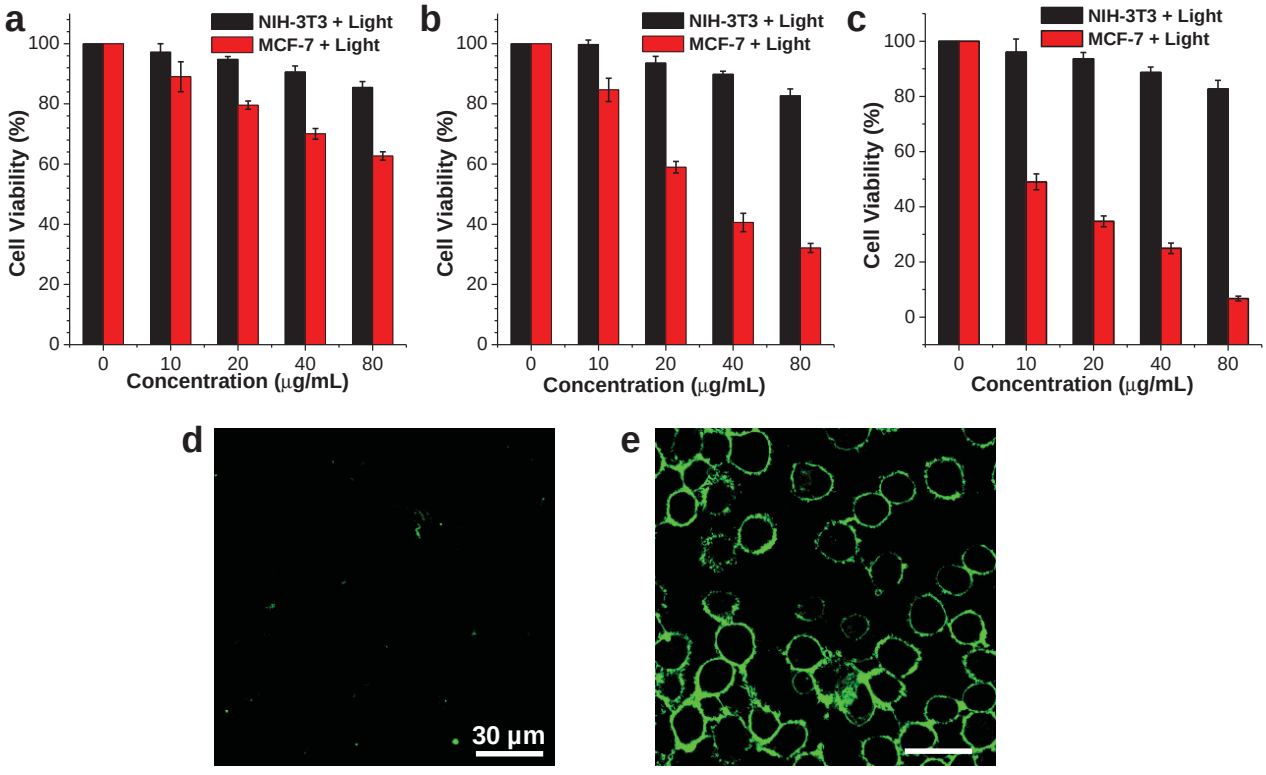

Figure 5. Viabilities of MCF-7 cancer cells and NIH-3T3 normal cells after incubation with a) AIE–TPP, b) AIE–FA, and c) FA–AIE–TPP dots at varied concentrations, followed by white light irradiation (250 mW cm^{-2}). d,e) Annexin V labeled MCF-7 cells after incubation with FA–AIE–TPP dots (20 μg mL^{-1}) without (d) or with (e) light irradiations (250 mW cm^{-2}). Panels (d) and (e) share the same scale bar.

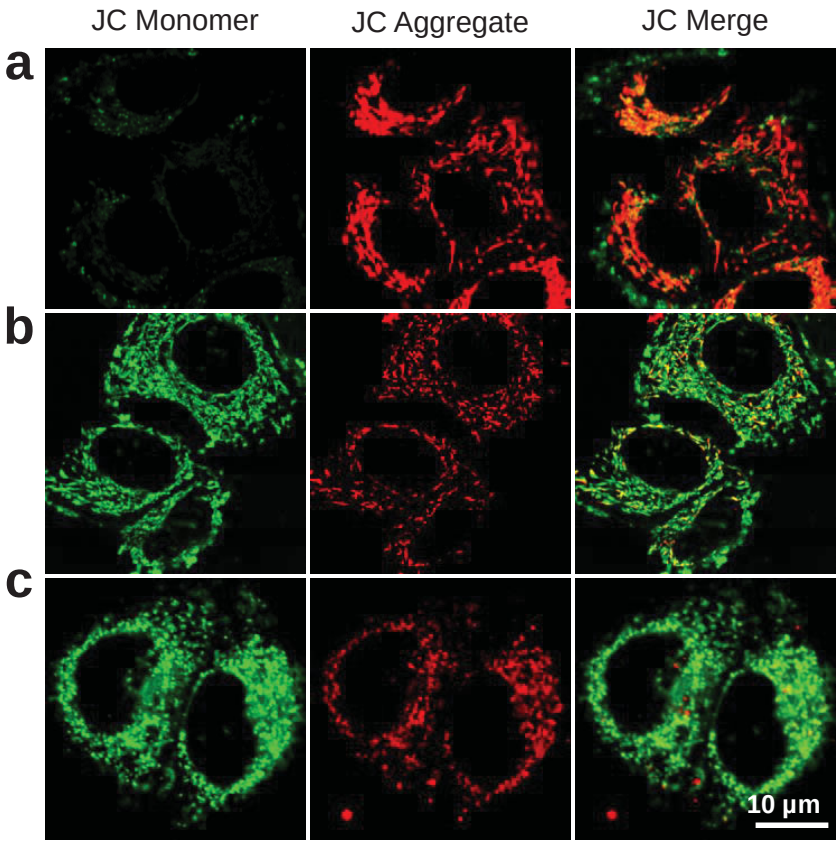

Figure 6. Mitochondrial potential changes of FA–AIE–TPP dots (20 μg mL^{-1}) treated MCF-7 cancer cells measured by JC-1 (2 μg mL^{-1}) after light irradiation (100 mW cm^{-2}) for a) 0, b) 5, and c) 10 min. All the images share the same scale bar.

should be due to the poor cellular uptake. As for MCF-7 cells, FA–AIE–TPP dots show the most efficient killing efficiency under light irradiation with a cell viability of less than 10% at the DPBA–TPE concentration of 80 μg mL^{-1}, while under the same condition, AIE–TPP and AIE–FA dots treated MCF-7 cells show cell viabilities of ≈60% and ≈32%, respectively. The half-maximal inhibitory concentration (IC_{50}) was further applied to quantify the anticancer efficiency of the three dots under light irradiation. The IC_{50} values are >80, ≈32, and ≈10 μg mL^{-1} for AIE–TPP, AIE–FA, and FA–AIE–TPP dots, respectively. As almost the same amount of AIE–FA and FA–AIE–TPP dots is internalized into MCF-7 cells as revealed by CLSM and flow cytometry (Figure 4 and Figure S6, Supporting Information), the lower IC_{50} of FA–AIE–TPP dots clearly indicates that localizing PS-loaded nanocarriers in mitochondria helps enhance anticancer effects of PDT. The comparison between AIE–TPP and FA–AIE–TPP dots also reveals that the increased cellular uptake of the latter helps increase the amount of NPs accumulated at mitochondria to yield enhanced PDT. Moreover, the killing efficiency of FA–AIE–TPP dots toward MCF-7 cells also increases with the exposure time and light power (Figure S9, Supporting Information). PDT-triggered cell death normally destroys the mitochondrial membrane and triggers the release of cytochrome, leading to apoptosis process. We used fluorescein isothiocyanate (FITC)-tagged Annexin V to differentiate apoptotic cells from viable ones. As shown in Figure 5d,e, incubating MCF-7 cells with FA–AIE–TPP dots in dark show almost no green fluorescence from Annexin V, as is observed, while upon light irradiation, bright green fluorescence originated from Annexin V can be observed from cellular membrane, indicating that MCF-7 cells undergo apoptosis process in the presence of FA–AIE–TPP dots and light irradiation.

It has been reported that PDT treatment on mitochondria can cause mitochondrial damage, leading to cell apoptosis and death. One of the characteristics of mitochondrial damage or dysfunction is the loss of mitochondrial membrane potential (MMP), which will trigger the release of cytochrome at the early stage of apoptosis.[50–52] We used a membrane-permeable JC-1 dye to monitor MMP changes during PDT treatment. JC-1 dye undergoes reversible fluorescence changes between its aggregate and monomer states. At high MMP level, JC-1 forms red emissive fluorescent aggregates on normal mitochondria, while it is shifted to green emissive monomer on depolarized mitochondria with low MMP. **Figure 6** shows the representative confocal images of JC-1 assays, and the green/red (G/R) ratio helps quantify the MMP loss of MCF-7 cells during PDT. The accumulation of FA–AIE–TPP dots in mitochondria in dark does not depolarize the mitochondrial membrane as evidenced by the dim green fluorescence and bright red fluorescence from JC-1 dye. Upon exposure to white light, the JC-1 staining changes, where green fluorescence increases at the expense of red fluorescence (G/R ratio changes from 0.46 to 3.59 and 4.37), indicate the loss of MMPs and damage of mitochondria upon light irradiation. In addition, irradiation of blank MCF-7 cancer cells does not cause obvious MMP changes (Figure S10, Supporting Information), further indicating that mitochondrial damage is due to the ROS generated by AIE dots under light illumination. It should be noted that the red fluorescence emitted from FA–AIE–TPP dots is still observable during PDT treatment, which provides the opportunity to visualize the morphology changes of mitochondria from characteristic tubular-like structure to dot-like structures after light irradiation.

As the powerhouse of cells, mitochondrion provides the major energy for cancer-cell activities, including proliferation, migration, and metastasis. It is postulated that the dysfunction of mitochondria highly affects the ATP production and hence the migration of cancer cells. A cell-scratch spatula method is used to study the effects of AIE dots on cell migration before and after light irradiation. A scratch was applied to the cell monolayer prior to 4 h incubation with these three AIE dots (20 μg mL^{-1} based on DPBA–TPE mass concentration) and light irradiation (100 mW cm^{-2}, 10 min). The migration ratio is determined by the number of cells migrated to the wound area after the PDT treatment to that of control cells without AIE dots treatment and light irradiation after 72 h post culture (**Figure 7**). The AIE dots and light irradiation do not affect the migration ability of NIH-3T3 cells, as they migrate into the wound area with a very high

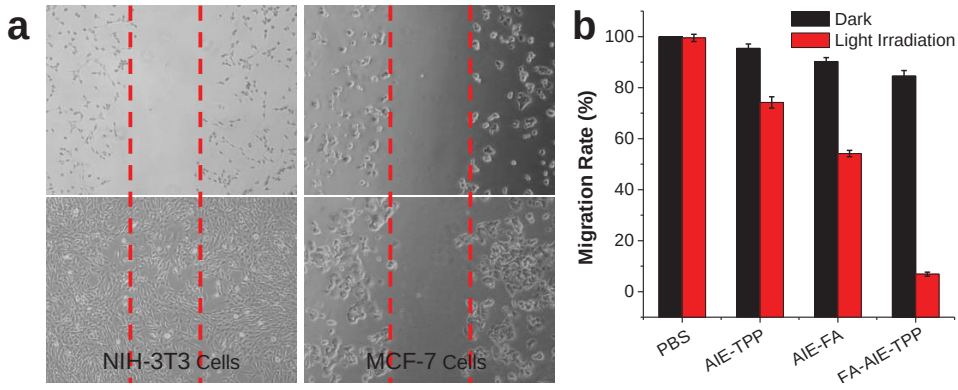

Figure 7. a) White field image of FA–AIE–TPP dots treated NIH-3T3 and MCF-7 cells before (up) and after 72 h culture (bottom). Both cells were incubated with FA–AIE–TPP dots (20 μg mL^{-1} based on DPBA–TPE mass concentration) for 4 h, followed by light exposure (100 mW cm^{-2}) for 10 min. b) The effects of AIE dots treatment on migration of MCF-7 cells with and without light irradiation.

migration ratio of ≈100%. On the other hand, AIE dots in dark do not affect the migration ability of MCF-7 cells, but further light irradiation is able to inhibit the wound closure of AIE dots treated MCF-7 cells, with migration ratios of 74.2%, 54.1%, and 6.8% for AIE–TPP, AIE–FA, and FA–AIE–TPP dots, respectively (Figure 7b and Figure S11, Supporting Information). As cancer cells are highly metastatic, the inhibition of migration should also contribute to the anticancer therapy.

3. Conclusion

In summary, we fabricated dual-targeted AIE dots with efficient ROS generation for FR-positive cancer cellular and mitochondrial dual-targeted image-guided PDT. The new AIE dots showed bright red fluorescence and efficient ROS generation under light irradiation. To specially target the mitochondria of a selective type of cancer cells, the AIE dot surfaces were decorated with folate acid and TPP. Folate acid promotes the cellular uptake to FR-positive cancer cells, and TPP drives AIE dots to accumulate in mitochondria. The generation of ROS at mitochondria is able to quickly depolarize and destroy the mitochondrial membrane, and largely affects cancer-cell migration ability. Cell viability studies revealed that dual-functionalized FA–AIE–TPP dots showed more efficient anticancer PDT effects than single-ligand-functionalized AIE–TPP or AIE–FA dots. Different from traditional approaches that require tedious processes to modify PSs for targeted PDT, this AIE dots strategy provides a new platform for cellular- and organelle-targeted image-guided PDT. Moreover, when the developed strategy is further applied to other imaging or therapeutic reagents, it should open new research opportunities in drug delivery and cancer therapy.

4. Experimental Section

Materials: 1,4-bis(Bromomethyl)-2,5-dimethoxybenzene (**2**),[87] 2,5-bimethoxybenzene-1,4-dicarboxaldehyde (**3**),[88] and *N*-(4-(1,2,2-triphenylvinyl)phenyl)benzenamine (**10**)[77] were prepared according to the literature. DSPE–PEG–NH_2, DSPE–PEG–FA, and DSPE–PEG were purchased from Avanti Polar Lipids, Inc. All the other chemicals and reagents were purchased from Sigma-Aldrich and used as received without further purification.

Characterization: ^{1}H NMR spectra were measured on a Bruker AV 300 or 400 spectrometer in CD_2Cl_2 by using tetramethylsilane (TMS; δ = 0) as internal reference. High-resolution mass spectra (HRMS) were recorded on a GCT premier CAB048 mass spectrometer operating in MALDI–TOF mode. The UV–vis and PL spectra were measured on UV-1700 (Shimadzu, Japan) and LS-55 (Perkin Elmer, USA) spectrometer, respectively. Laser light scattering with a particle size analyzer (90 Plus, Brookhaven Instruments Co., USA) was used to determine the hydrodynamic diameters of AIE dots. Zeta potential of AIE dots was determined by Zetasizer (Malvern, UK). HR-TEM (JEM-2010F, JEOL, Japan) was used to study the morphology and size of AIE dots.

Preparation of DPBA–TPE: A dry ethanol solution (30 mL) of sodium hydroxide (40 mg) was added to a mixture of 4-bromophenylacetonitrile (873 mg, 4.5 mmol) and 2,5-bimethoxybenzene-1,4-dicarboxaldehyde (388 mg, 2 mmol) under a nitrogen atmosphere. The reaction mixture was stirred for 12 h at room temperature, and the precipitate was filtered out and washed with water and DCM. An orange powder (**5**) was obtained in 81.9% yield (904 mg). Compound **5** (200 mg, 0.364 mmol) was reacted with **10** (381 mg, 0.9 mmol) in the presence of $Pd(OAc)_2$ (11.2 mg, 0.05 mmol), Cs_2CO_3 (487 mg, 1.5 mmol), P(*t*-Bu)$_3$ (30.3 mg, 0.15 mmol), and toluene (40 mL) at 110 °C for 24 h under a nitrogen atmosphere. Water (30 mL) and chloroform (300 mL) were then added after cooling to room temperature. The obtained organic layer was washed with brine, dried by anhydrous $MgSO_4$, and further dried under reduced pressure. Column chromatography on silica gel using hexane/DCM as eluent was then applied to purify the crude product. The afforded DPBA–TPE was used as a red solid in 68% yield (305 mg). ^{1}H NMR (400 MHz, CD_2Cl_2), δ (TMS, ppm): 7.90 (s, 2H), 7.88 (s, 2H), 7.55 (d, J = 8.8 Hz, 4H), 7.30 (t, J = 8.0 Hz, 4H), 7.18–7.02 (m, 40H), 6.94 (d, J = 8.4 Hz, 4H), 6.85 (d, J = 8.4 Hz, 4H), 3.94 (s, 6H). ^{13}C NMR (75 MHz, $CDCl_3$), δ (TMS, ppm): 152.32, 149.09, 147.25, 145.65, 144.32, 144.14, 143.92, 141.36, 140.98, 139.70, 133.78, 132.66, 131.67, 131.64, 131.61, 129.79, 128.19, 128.05, 128.02, 127.25, 126.86, 126.83, 126.76, 125.94, 125.47, 124.34, 124.22, 122.76, 118.79, 111.89, 110.58, 56.74. HRMS (MALDI–TOF, m/z): [M^+] calcd for $C_{90}H_{66}N_4O_2$, 1234. 5186; found, 1234.5192. Anal. calcd for $C_{90}H_{66}N_4O_2$: C, 87.49; H, 5.38; N, 4.53; O, 2.59. found: C, 87.61; H, 5.33; N, 4.52.

Preparation of DPBA–TPE Nanoaggregates: DPBA–TPE was fully dissolved in THF to prepare the stock (100 × 10^{-6} M). Appropriate amounts of the THF stock solution were then mixed with different volumes of MilliQ water under vigorous stirring to reach the final concentration of 10 × 10^{-6} M with different water fraction (0–90 vol%). The PL spectra of these mixtures were then measured by LS-55 spectrometer.

ROS Generation Measurement: The ROS generation of DPBA–TPE aggregates or AIE dots under light irradiation was measured using DCFH as the indicator. The PL spectra of the mixture of DPBA–TPE (10×10^{-6} M) and DCFH (2×10^{-6} M) were measured before and after exposure to white light irradiation (250 mW cm^{-2}) upon excitation at 460 nm. The increase of fluorescence intensity at 530 nm is the indication of ROS generation in solution. The same experimental procedures were applied to AIE dots.

Preparation of AIE–FA Dots: To synthesize AIE–FA dots, a THF solution (1 mL) containing DPBA–TPE (0.5 mg), DSPE–PEG–FA (0.5 mg), and DSPE–PEG (0.5 mg) was poured into water (10 mL) under sonication using a microtip probe sonicator at 12 W output (XL2000, Misonix Incorporated, NY). The mixture was further placed in dark in fume hood for THF evaporation at 600 rpm overnight, and concentrated by centrifuge.

Preparation of AIE–TPP Dots: To synthesize AIE–TPP dots, DSPE–PEG–NH_2 (0.5 mg) was used to replace DSPE–PEG–FA (0.5 mg) during the nanoparticle formation. The resultant AIE dots suspension with amino group at surface was reacted with excess TPP. AIE–TPP dots were then dialyzed against water with 6–8 kDa membrane to remove excess TPP.

Preparation of FA–AIE–TPP Dots: To synthesize FA–AIE–TPP dots, DSPE–PEG–FA (0.5 mg) and DSPE–PEG–NH_2 (0.5 mg) were used as the matrix during dots formation. The AIE dots suspension was then reacted with TPP. FA–AIE–TPP dots were then dialyzed against water using 6–8 kDa membrane to remove excess TPP.

Confocal Imaging: NIH-3T3 normal cells and MCF-7 cancer cells were cultured in eight-well chamber (LAB-TEK, Chambered Coverglass System) at 37 °C. After 80% confluence, the cells were incubated for 4 h with these AIE dots (20 μg mL^{-1} based on DPBA–TPE mass concentration) suspended in cell culture medium, and then washed twice with PBS. To label mitochondria, the cells were further incubated with MitoTracker Green (Invitrogen, 200×10^{-9} M) for 20 min. After washing, the cells were immediately imaged by CLSM. The red fluorescence from AIE dots was acquired above 650 nm upon excitation at 534 nm. The green fluorescence from MitoTracker Green was obtained between 505 to 560 nm upon excitation at 488 nm.

Measurement of Mitochondrial Membrane Potential: JC-1 dye (Invitrogen) was used to measure MMP changes during PDT treatment. After 4 h incubation of MCF-7 cells with these AIE dots (20 μg mL^{-1} based on DPBA–TPE mass concentration) suspended in cell culture medium. The cells were washed and exposed to light irradiation (100 mW cm^{-2}) for 0, 5, and 10 min. MCF-7 cells were incubated with JC-1 dyes (2 μg mL^{-1}) for 20 min. After washing, the cells were immediately imaged by CLSM. Upon excitation at 488 nm, the green signal was collected between 505 and 525 nm, and the red signal was collected above 590 nm.

Flow Cytometry: NIH-3T3 normal cells and MCF-7 cancer cells were cultured in a six-well plate at 37 °C. After 80% confluence, the cells were incubated with these AIE dots (20 μg mL^{-1} based on DPBA–TPE mass concentration) suspended in cell culture medium for 4 h. The cells were then harvested by trypsin, and resuspended in 1× PBS. Cyan-LX (DakoCytomation) was then used to access the fluorescence intensities of cells, where 10 000 events were counted for the histogram analysis.

Cell Migration Assay: NIH-3T3 and MCF-7 cells were cultured into six-well plates and grown for 24 h. Cell scratch spatula were applied to make a scratch in the cell monolayer. After rinsing the cells with PBS, the photographs of the scratches were taken using a microscope with a 10× objection (Nikon–Ti–U). The cells were then treated with AIE dots (20 μg mL^{-1} based on DPBA–TPE mass concentration) for 4 h and followed by light irradiation (100 mW cm^{-2}, 10 min), the cells were further cultured for 72 h, after which the pictures were taken again. The migration ratio is determined by the number of cells migrated to wound area after PDT treatment to that of control cells without AIE dots treatment and light irradiation after 72 h.

Cytotoxicity Studies: The viability of NIH-3T3 and MCF-7 cells was evaluated using MTT assays. Both cells were seeded in 96-well plates (Costar, IL, USA) at an intensity of 4×10^4 cells mL^{-1}, respectively. After 24 h incubation, AIE dots in DMEM suspension at various concentrations were then added into each well. After 4 h incubation, the AIE dot suspensions were replaced by fresh cell culture medium. The selected wells were exposed to light irradiation (100 mW cm^{-2}, 10 min), and further cultured for 24 h. In the parallel experiment, both cell lines were treated with AIE dots for 24 h in dark. The cells were then incubated with MTT solution (0.5 mg mL^{-1}, 100 μL per well) for 3 h. After removal of MTT, filtered DMSO was then added (100 μL per well) and the plate was gently shaken for 10 min at room temperature to dissolve all the precipitates formed. Microplate reader (Genios Tecan) was then used to access the absorbance of MTT at 570 nm. Cell viability was determined by the ratio of the absorbance of the cells incubated with AIE dots to that of the cells incubated with culture medium only. The same experiment procedures were repeated by fixing the AIE dots concentration with varied light power or exposure time.

Supporting Information

Supporting Information is available from the Wiley Online Library or from the author.

Acknowledgements

G.F. and W.Q. contributed equally to this work. The authors are grateful to the Singapore National Research Foundation (R279-000-444-281), SMART (R279-000-378-592), the Economic Development Board (Singapore–Peking–Oxford Research Enterprise, COY-15-EWI-RCFSA/N197-1), and Institute of Materials Research and Engineering of Singapore (IMRE/14-8P1110) for financial support. The authors declare no competing financial interest.

Received: June 8, 2015
Revised: June 18, 2015
Published online: October 19, 2015

[1] X. Wang, S. Peralta, C. T. Moraes, in *Advances in Cancer Research*, (Eds. K. Tew, P. Fisher), Academic Press, Oxford, **2013**, *119*, 127.
[2] L. Rajendran, H.-J. Knolker, K. Simons, *Nat. Rev. Drug Discov.* **2010**, *9*, 29.
[3] S. Weigl, A. Paradiso, S. Tommasi, *Curr. Genomics* **2013**, *14*, 195.
[4] K. K. Y. Wong, X. L. Liu, *Pediatr. Surg. Int.* **2012**, *28*, 943.
[5] C. S. Lim, *Adv. Drug Delivery Rev.* **2007**, *59*, 697.
[6] V. P. Torchilin, *Annu. Rev. Biomed. Eng.* **2006**, *8*, 343.
[7] B. C. Dickinson, C. J. Chang, *J. Am. Chem. Soc.* **2008**, *130*, 9638.
[8] N. M. Sakhrani, H. Padh, *Drug Des., Dev. Ther.* **2013**, *7*, 585.
[9] S. P. Y. Li, C. T. S. Lau, M. W. Louie, Y. W. Lam, S. H. Cheng, K. K. W. Lo, *Biomaterials* **2013**, *34*, 7519.
[10] P. Prasad, I. Khan, P. Kondaiah, A. R. Chakravarty, *Chem.-Eur. J.* **2013**, *19*, 17445.
[11] J. Xu, F. Zeng, H. Wu, C. Hu, S. Wu, *Biomacromolecules* **2014**, *15*, 4249.
[12] P. Rajaputra, G. Nkepang, R. Watley, Y. You, *Bioorg. Med. Chem.* **2013**, *21*, 379.
[13] Q. Hu, M. Gao, G. Feng, B. Liu, *Angew. Chem. Int. Ed.* **2014**, *53*, 14225.
[14] S. V. Boddapati, G. G. M. D'Souza, S. Erdogan, V. P. Torchilin, V. Weissig, *Nano Lett.* **2008**, *8*, 2559.
[15] A. Sharma, G. M. Soliman, N. Al-Hajaj, R. Sharma, D. Maysinger, A. Kakkar, *Biomacromolecules* **2011**, *13*, 239.
[16] M. Breunig, S. Bauer, A. Goepferich, *Eur. J. Pharm. Biopharm.* **2008**, *68*, 112.
[17] S. Ganta, H. Devalapally, A. Shahiwala, M. Amiji, *J. Controlled Release* **2008**, *126*, 187.

[18] L. Jabr-Milane, L. van Vlerken, H. Devalapally, D. Shenoy, S. Komareddy, M. Bhavsar, M. Amiji, *J. Controlled Release* **2008**, *130*, 121.
[19] D. Peer, J. M. Karp, S. Hong, O. C. Farokhzad, R. Margalit, R. Langer, *Nat. Nanotechnol.* **2007**, *2*, 751.
[20] R. Savić, L. Luo, A. Eisenberg, D. Maysinger, *Science* **2003**, *300*, 615.
[21] G. G. M. D'Souza, M. A. Wagle, V. Saxena, A. Shah, *Biochem. Biophys. Acta-Bioenerg.* **2011**, *1807*, 689.
[22] A. Sharma, G. M. Soliman, N. Al-Hajaj, R. Sharma, D. Maysinger, A. Kakkar, *Biomacromolecules* **2012**, *13*, 239.
[23] S. Marrache, S. Dhar, *Proc. Natl. Acad. Sci. USA* **2012**, *109*, 16288.
[24] T. Paunesku, S. Vogt, B. Lai, J. Maser, N. Stojićević, K. T. Thurn, C. Osipo, H. Liu, D. Legnini, Z. Wang, C. Lee, G. E. Woloschak, *Nano Lett.* **2007**, *7*, 596.
[25] L. Wang, Y. Liu, W. Li, X. Jiang, Y. Ji, X. Wu, L. Xu, Y. Qiu, K. Zhao, T. Wei, Y. Li, Y. Zhao, C. Chen, *Nano Lett.* **2010**, *11*, 772.
[26] K. Esumi, H. Houdatsu, T. Yoshimura, *Langmuir* **2004**, *20*, 2536.
[27] K. Esumi, N. Takei, T. Yoshimura, *Colloids Surf., B* **2003**, *32*, 117.
[28] Y. Yamada, R. Furukawa, Y. Yasuzaki, H. Harashima, *Mol. Ther.* **2011**, *19*, 1449.
[29] Y. Yamada, E. Kawamura, H. Harashima, *J. Nanopart. Res.* **2012**, *14*, 1.
[30] E. Kawamura, Y. Yamada, Y. Yasuzaki, M. Hyodo, H. Harashima, *J. Biosci. Bioeng.* **2013**, *116*, 634.
[31] R. Mo, Q. Sun, J. Xue, N. Li, W. Li, C. Zhang, Q. Ping, *Adv. Mater.* **2012**, *24*, 3659.
[32] J. Xu, F. Zeng, H. Wu, C. Wu, S. Wu, *ACS. Appl. Mater. Interfaces* **2015**, *7*, 9287.
[33] A. P. Castano, T. N. Demidova, M. R. Hamblin, *Photodiagn. Photodyn. Ther.* **2004**, *1*, 279.
[34] F. H. van Duijnhoven, R. I. J. M. Aalbers, J. P. Rovers, O. T. Terpstra, P. J. K. Kuppen, *Immunobiology* **2003**, *207*, 105.
[35] M. B. Vrouenraets, G. W. M. Visser, F. A. Stewart, M. Stigter, H. Oppelaar, P. E. Postmus, G. B. Snow, G. A. M. S. van Dongen, *Cancer Res.* **1999**, *59*, 1505.
[36] T. Nakajima, K. Sano, M. Mitsunaga, P. L. Choyke, H. Kobayashi, *Cancer Res.* **2012**, *72*, 4622.
[37] T. Nakajima, K. Sano, P. L. Choyke, H. Kobayashi, *Theranostics* **2013**, *3*, 357.
[38] R. Hudson, M. Carcenac, K. Smith, L. Madden, O. J. Clarke, A. Pelegrin, J. Greenman, R. W. Boyle, *Br. J. Cancer* **2005**, *92*, 1442.
[39] D. E. J. G. J. Dolmans, D. Fukumura, R. K. Jain, *Nat. Rev. Cancer* **2003**, *3*, 380.
[40] A. P. Castano, P. Mroz, M. R. Hamblin, *Nat. Rev. Cancer* **2006**, *6*, 535.
[41] E. S. Marmur, C. D. Schmults, D. J. Goldberg, *Dermatol. Surg.* **2004**, *30*, 264.
[42] R. R. Allison, C. H. Sibata, *Photodiagn. Photodyn. Ther.* **2010**, *7*, 61.
[43] J. Moan, K. Berg, *Photochem. Photobiol.* **1991**, *53*, 549.
[44] E. Skovsen, J. W. Snyder, J. D. C. Lambert, P. R. Ogilby, *J. Phys. Chem. B* **2005**, *109*, 8570.
[45] S. Kim, T. Tachikawa, M. Fujitsuka, T. Majima, *J. Am. Chem. Soc.* **2014**, *136*, 11707.
[46] G. A. M. S. van Dongen, G. W. M. Visser, M. B. Vrouenraets, *Adv. Drug Delivery Rev.* **2004**, *56*, 31.
[47] J. P. Celli, B. Q. Spring, I. Rizvi, C. L. Evans, K. S. Samkoe, S. Verma, B. W. Pogue, T. Hasan, *Chem. Rev.* **2010**, *110*, 2795.
[48] J.-O. Yoo, K.-S. Ha, *International Review of Cell and Molecular Biology*, Academic Press, Tennessee, USA, **2012**, Vol. *295*, 139.
[49] P. R. Ogilby, *Chem. Soc. Rev.* **2010**, *39*, 3181.
[50] M. Lam, N. L. Oleinick, A.-L. Nieminen, *J. Biol. Chem.* **2001**, *276*, 47379.
[51] R. Hilf, *J. Bioenerg. Biomembr.* **2007**, *39*, 85.
[52] E. J. Ngen, P. Rajaputra, Y. You, *Bioorg. Med. Chem.* **2009**, *17*, 6631.
[53] D. Kessel, Y. Luo, *Cell Death Differ.* **1999**, *6*, 28.
[54] J. Morgan, A. R. Oseroff, *Adv. Drug Delivery Rev.* **2001**, *49*, 71.
[55] W. Lei, J. Xie, Y. Hou, G. Jiang, H. Zhang, P. Wang, X. Wang, B. Zhang, *J. Photochem. Photobiol. B: Biol.* **2010**, *98*, 167.
[56] M. G. Alvarez, F. Príncipe, M. E. Milanesio, E. N. Durantini, V. Rivarola, *Int. J. Biochem. Cell Biol.* **2005**, *37*, 2504.
[57] L. E. Bennett, K. P. Ghiggino, R. W. Henderson, *J. Photochem. Photobiol. B: Biol.* **1989**, *3*, 81.
[58] S. Y. Park, H. J. Baik, Y. T. Oh, K. T. Oh, Y. S. Youn, E. S. Lee, *Angew. Chem. Int. Ed.* **2011**, *50*, 1644.
[59] U. Siggel, U. Bindig, C. Endisch, T. Komatsu, E. Tsuchida, J. Voigt, J. H. Fuhrhop, *Ber. Bunseng. Phys. Chem.* **1996**, *100*, 2070.
[60] D. Ding, K. Li, B. Liu, B. Z. Tang, *Acc. Chem. Res.* **2013**, *46*, 2441.
[61] Y. Hong, J. W. Y. Lam, B. Z. Tang, *Chem. Commun.* **2009**, 4332.
[62] Y. Hong, J. W. Y. Lam, B. Z. Tang, *Chem. Soc. Rev.* **2011**, *40*, 5361.
[63] Z. Zhao, W. Y. Lam, J. Zhong, B. Tang, *Curr. Org. Chem.* **2010**, *14*, 2109.
[64] J. Liu, J. Y. Lam, B. Tang, *J. Inorg. Organometal. Polym. Mater.* **2009**, *19*, 249.
[65] W. Z. Yuan, P. Lu, S. Chen, J. W. Y. Lam, Z. Wang, Y. Liu, H. S. Kwok, Y. Ma, B. Z. Tang, *Adv. Mater.* **2010**, *22*, 2159.
[66] Z. Chi, X. Zhang, B. Xu, X. Zhou, C. Ma, Y. Zhang, S. Liu, J. Xu, *Chem. Soc. Rev.* **2012**, *41*, 3878.
[67] J. Liang, B. Z. Tang, B. Liu, *Chem. Soc. Rev.* **2015**, *44*, 2798.
[68] J. Mei, Y. Hong, J. W. Y. Lam, A. Qin, Y. Tang, B. Z. Tang, *Adv. Mater.* **2014**, *26*, 5429.
[69] R. Hu, N. L. C. Leung, B. Z. Tang, *Chem. Soc. Rev.* **2014**, *43*, 4494.
[70] R. T. K. Kwok, C. W. T. Leung, J. W. Y. Lam, B. Z. Tang, *Chem. Soc. Rev.* **2015**, *44*, 4228.
[71] H. Shi, J. Liu, J. Geng, B. Z. Tang, B. Liu, *J. Am. Chem. Soc.* **2012**, *134*, 9569.
[72] Y. Yuan, C.-J. Zhang, M. Gao, R. Zhang, B. Z. Tang, B. Liu, *Angew. Chem. Int. Ed.* **2015**, *54*, 1780.
[73] Y. Yuan, R. T. K. Kwok, B. Z. Tang, B. Liu, *J. Am. Chem. Soc.* **2014**, *136*, 2546.
[74] K. Li, D. Ding, Q. Zhao, J. Sun, B. Tang, B. Liu, *Sci. China Chem.* **2013**, *56*, 1228.
[75] W. Qin, K. Li, G. Feng, M. Li, Z. Yang, B. Liu, B. Z. Tang, *Adv. Funct. Mater.* **2014**, *24*, 635.
[76] K. Li, Z. Zhu, P. Cai, R. Liu, N. Tomczak, D. Ding, J. Liu, W. Qin, Z. Zhao, Y. Hu, X. Chen, B. Z. Tang, B. Liu, *Chem. Mater.* **2013**, *25*, 4181.
[77] K. Li, W. Qin, D. Ding, N. Tomczak, J. Geng, R. Liu, J. Liu, X. Zhang, H. Liu, B. Liu, B. Z. Tang, *Sci. Rep.* **2013**, *3*, 1150.
[78] G. Feng, C. Y. Tay, Q. X. Chui, R. Liu, N. Tomczak, J. Liu, B. Z. Tang, D. T. Leong, B. Liu, *Biomaterials* **2014**, *35*, 8669.
[79] D. Ding, C. C. Goh, G. Feng, Z. Zhao, J. Liu, R. Liu, N. Tomczak, J. Geng, B. Z. Tang, L. G. Ng, B. Liu, *Adv. Mater.* **2013**, *25*, 6083.
[80] Y. Yuan, G. Feng, W. Qin, B. Z. Tang, B. Liu, *Chem. Commun.* **2014**, *50*, 8757.
[81] X. Zhang, X. Zhang, L. Tao, Z. Chi, J. Xu, Y. Wei, *J. Mater. Chem. B* **2014**, *2*, 4398.
[82] F. Hu, Y. Huang, G. Zhang, R. Zhao, H. Yang, D. Zhang, *Anal. Chem.* **2014**, *86*, 7987.
[83] G. Feng, K. Li, J. Liu, D. Ding, B. Liu, *Small* **2014**, *10*, 1212.
[84] K. Li, B. Liu, *Chem. Soc. Rev.* **2014**, *43*, 6570.
[85] R. W. Horobin, S. Trapp, V. Weissig, *J. Controlled Rel.* **2007**, *121*, 125.
[86] R. A. J. Smith, C. M. Porteous, A. M. Gane, M. P. Murphy, *Proc. Natl. Acad. Sci. USA* **2003**, *100*, 5407.
[87] I. Brehm, S. Hinneschiedt, H. Meier, *Eur. J. Org. Chem.* **2002**, 3162.
[88] P. Shao, Z. Li, J. L. Luo, H. L. Wang, J. G. Qin, *Synthetic. Commun.* **2005**, *35*, 49.
[89] J. S. Modica-Napolitano, J. R. Aprille, *Adv. Drug. Del. Rev.* **2001**, *49*, 63.